Supporting Information

Pressure-controlled oxygen activation at single metal atom sites in a manganese-cobalt coordination network on graphene: from triplet-singlet spin transition to superoxo dissociation.

Asha Yadav,[a] Stefania Baronio,[b] Michela De Col,[b] Danilo Comini,[b] Valentin Mischke,[c] Alessandro Namar,[b] Nikolay Vinogradov,[d] Mattia Scardamaglia,[d] Mirko Cinchetti,[c] Giovanni Zamborlini,[c][e] Paolo Giannozzi,[a][f]* Erik Vesselli[b][g][h]*

[a]Department of Mathematics, Computer Science, and Physics, University of Udine, 33100 Udine, Italy

[b]Department of Physics University of Trieste via A. Valerio 2, 34127 Trieste, Italy

[c]Department of Physics, TU Dortmund University, 44227 Dortmund, Germany

[d]MAX IV Laboratory, Lund University, 22100 Lund, Sweden

[e]Institute of Physics, NAWI Graz, University of Graz, Universitätsplatz 5, 8010 Graz, Austria

[f]CNR – Istituto Officina dei Materiali (IOM), SISSA, 34136 Trieste, Italy

[g]CNR – Istituto Officina dei Materiali (IOM), S.S. 14 km 163.5, Area Science Park, 34149 Basovizza, Trieste, Italy

[h]Center for Energy, Environment and Transport Giacomo Ciamician, University of Trieste, 34127 Trieste, Italy

*corresponding authors' e-mails: evesselli@units.it, paolo.giannozzi@uniud.it

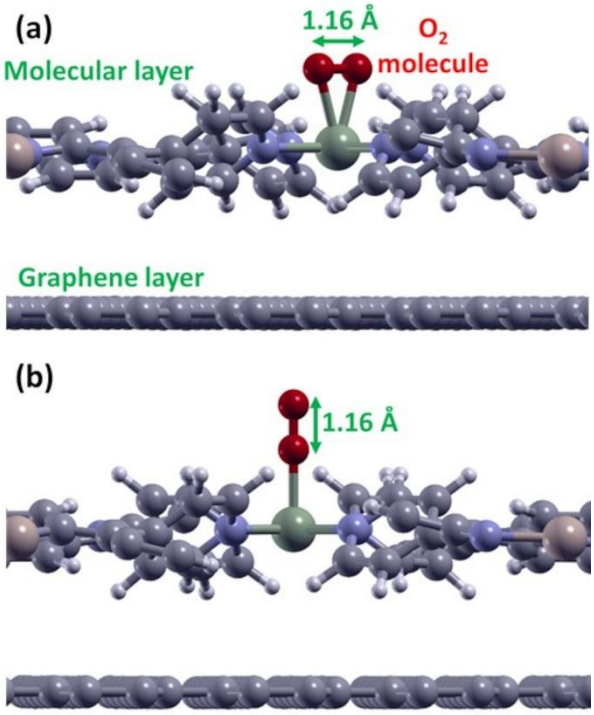

Figure S1. Starting structures of the O_2 approach to the Co site for the DFT simulations in two different configurations, with the internal O-O bond length contracted down to 1.16 Å: (a) H-conf and (b) V-conf.

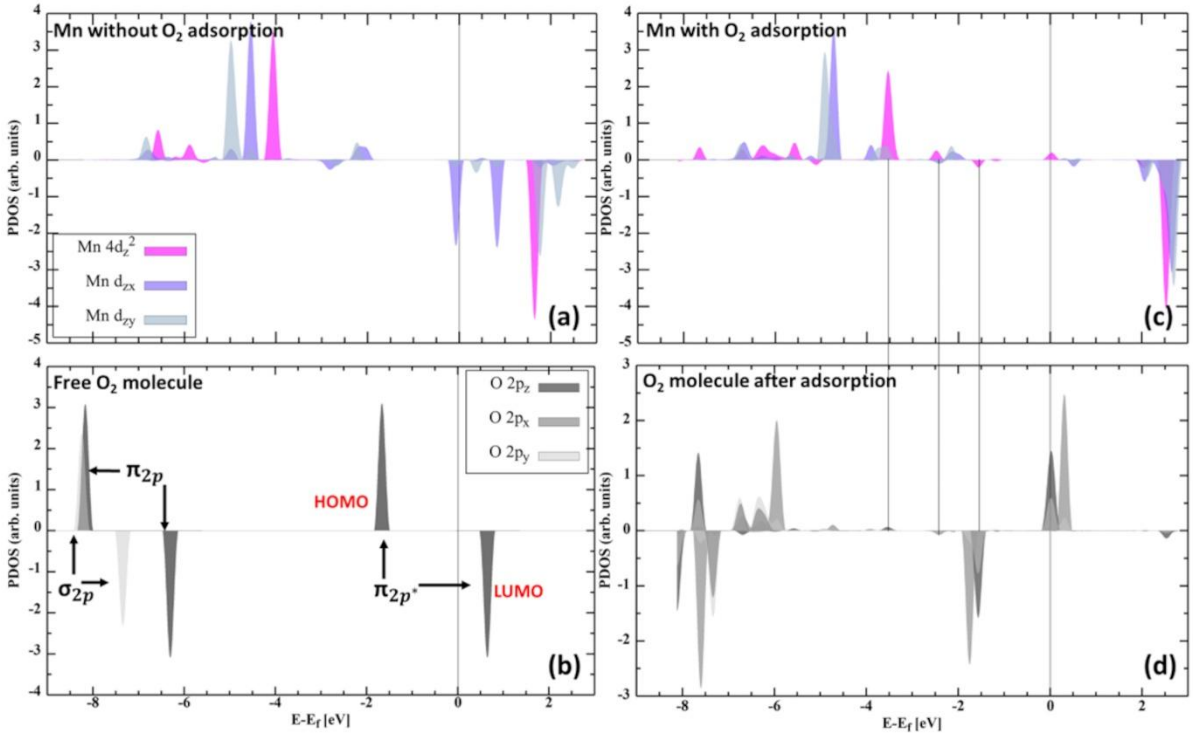

Figure S2. Atom/orbital projected, spin resolved density of states plot for (a,c) Mn 3*d* and (b,d) O 2*p* of the free O_2 molecule before (a,b) and after (c,d) relaxation**.** Since the O_2 molecule interacts with Mn along the z-direction, for simplicity, only z-components of the Mn 3d level are displayed.

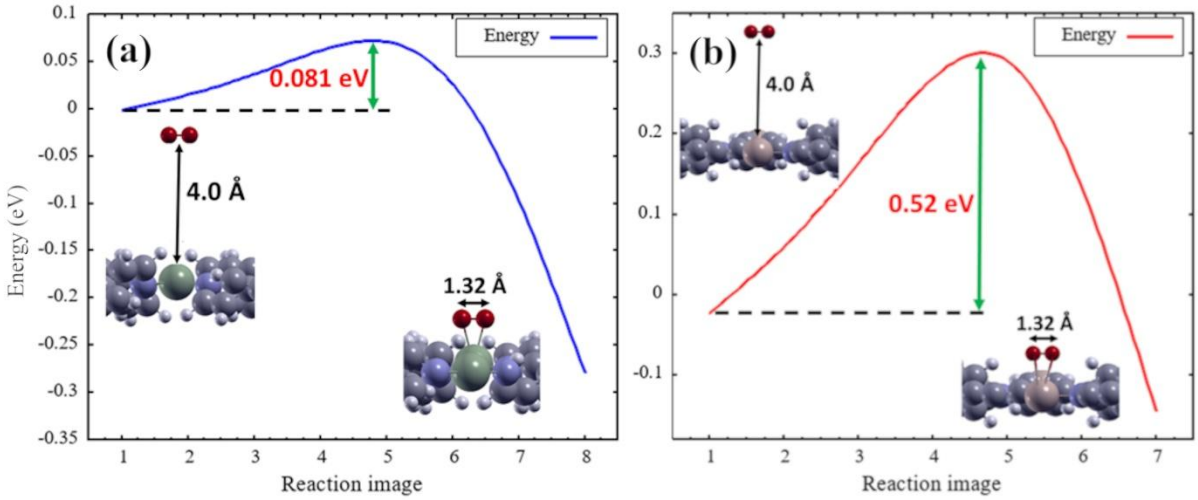

Figure S3. Reaction energy profiles along the vertical approach paths for the horizontal O_2 configurations at the (a) Co and (b) Mn sites. The reaction pathway is obtained with the nudged elastic band (NEB) method with 7 or 8 different configurations (images). The first image corresponds to an unbound O_2 molecule, the last one to the O_2 molecule bound in the horizontal configuration. Mind the different energy scales in the two panels.

Computational description of the O_2 interaction with the bimetallic CoTPyP-Mn layer on graphene.

With reference to adsorption sites and energies, we also modeled and evaluated O_2 adsorption at the Co site of the CoTPyP–Mn/Gr system. A comparison between O_2 adsorption at the central core Co site and the peripheral Co site reveals a significant difference in adsorption energy. For the central core Co site, O_2 adsorption in both horizontal and vertical configurations exhibits lower adsorption energies (−0.574 eV and −0.484 eV, respectively) compared to those at the peripheral Co sites. Furthermore, the larger Co–O bond distance (2.95 ÷ 3.34 Å), shorter O–O bond length (1.24 Å), and a magnetic moment of 0.52 μB on each O atom of O_2, collectively indicate a weaker interaction between O_2 and the Co site in the CoTPyP–Mn/Gr system.

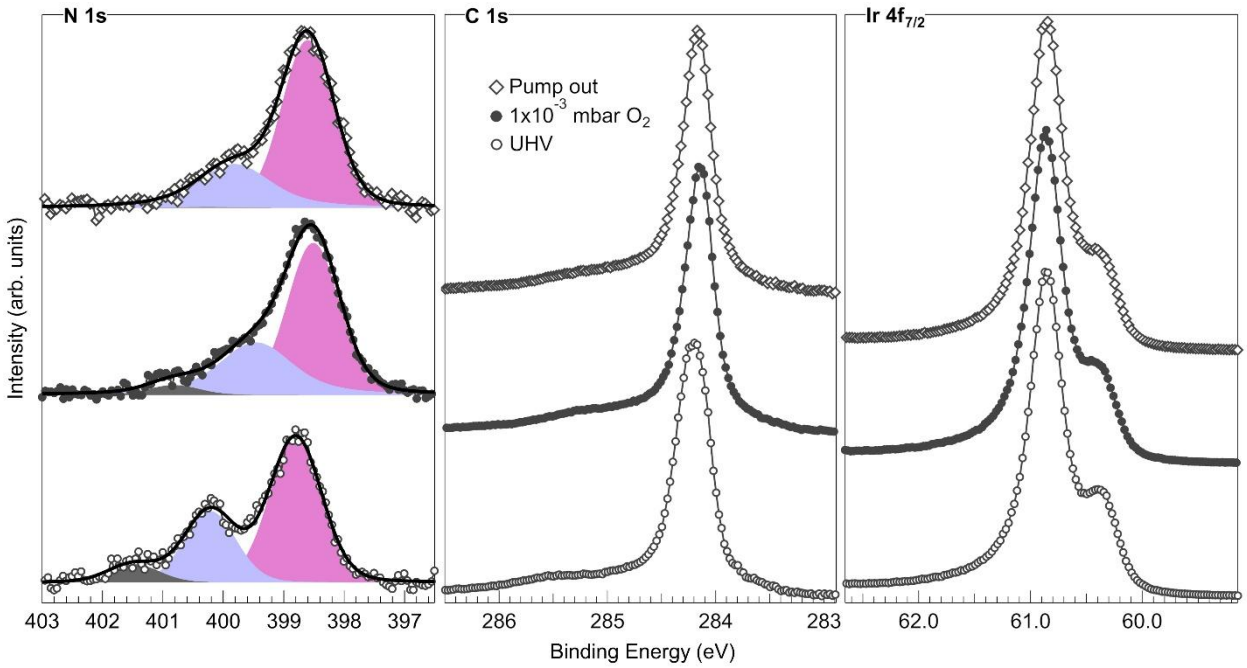

Figure S4. Core level spectra of a monolayer MnTPyP-Co/Gr (from bottom to top) as grown in UHV, in 10^{-3} mbar O_2 and after recovering UHV conditions. The photon energies employed to measure the spectra are 514 eV for N 1*s* and 400 eV for C 1*s* and Ir $4f_{7/2}$, respectively.

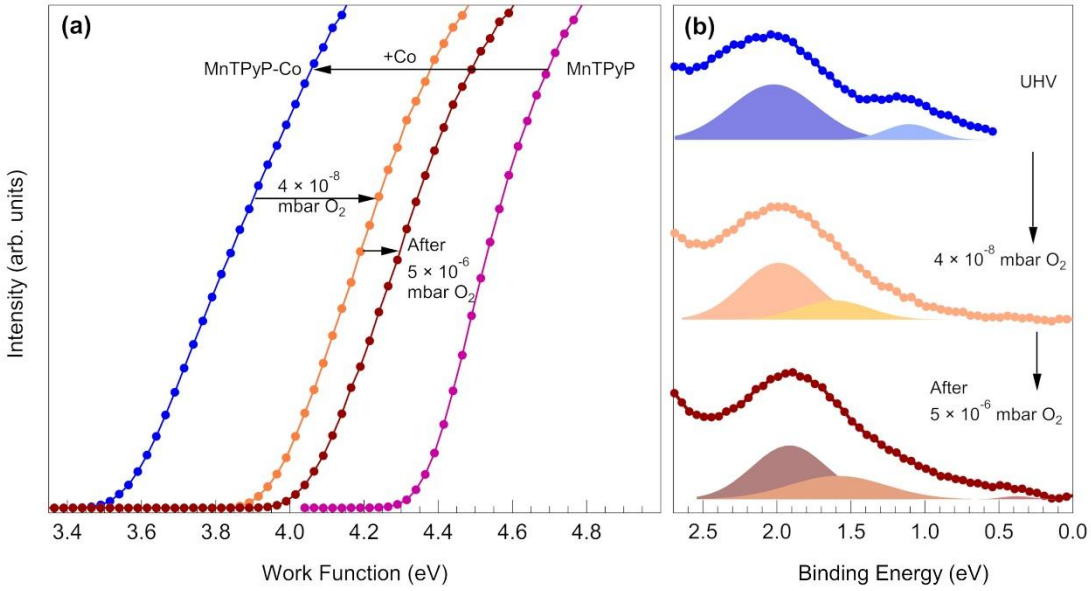

Figure S5. (a) Secondary electron onsets yielding the work function evolution for 1 ML MnTPyP/Gr in UHV, after addition of Co, upon exposure to 4×10^{-8} mbar O_2 and after 30 minutes at 5×10^{-6} mbar O_2; (b) electron density curves (EDCs) of 1 ML MnTPyP-Co/Gr in UHV, in 4×10^{-8} mbar O_2 and after 30 minutes at 5×10^{-6} mbar O_2 after subtraction of the graphene spectrum contribution. Both measurements were performed using the He(I) line of a monochromatized helium lamp ($h\nu$ = 21.2 eV). The features observed in each spectrum are fitted with Gaussian profiles, to extract their binding energy position.

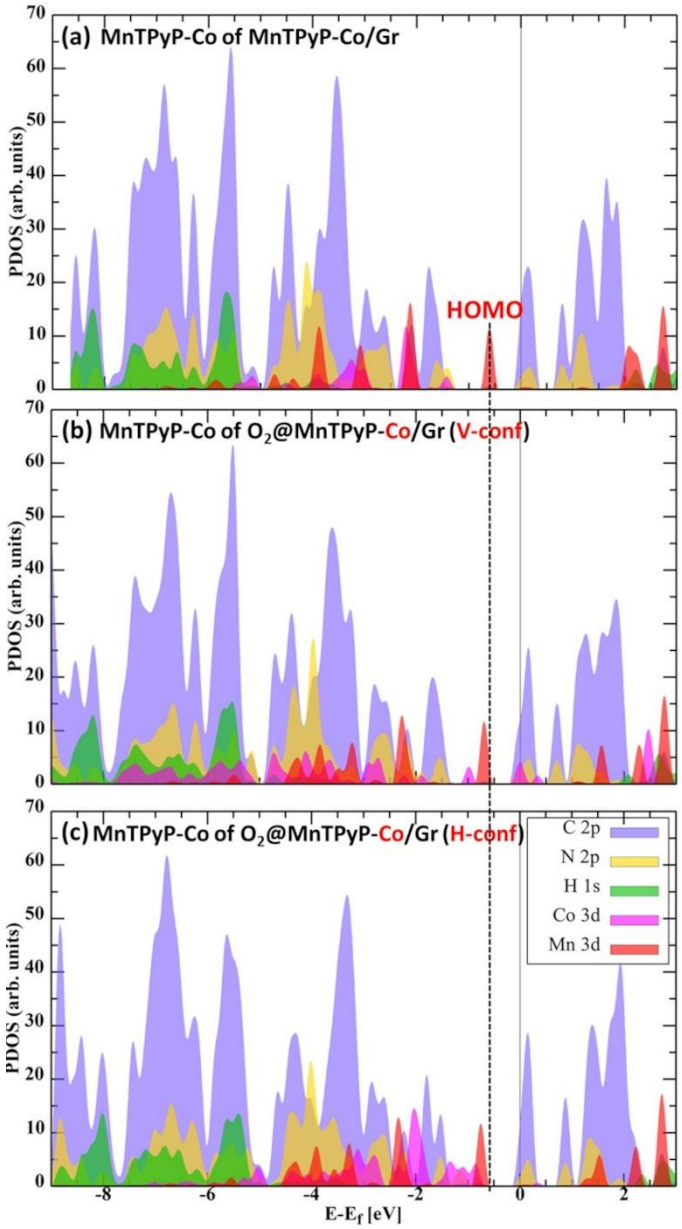

Figure S6. Projected density of states of (a) the MnTPyP-Co complex of MnTPyP-Co/Gr, (b) the MnTPyP-Co complex with O_2 adsorbed at the Co site in V-conf on MnTPyP-Co/Gr, and (c) the MnTPyP-Co complex with O_2 adsorbed at the Co site in H-conf on MnTPyP-Co/Gr. The black dashed line shows the position of the HOMO in the O_2 adsorbed system with respect to the pristine case.

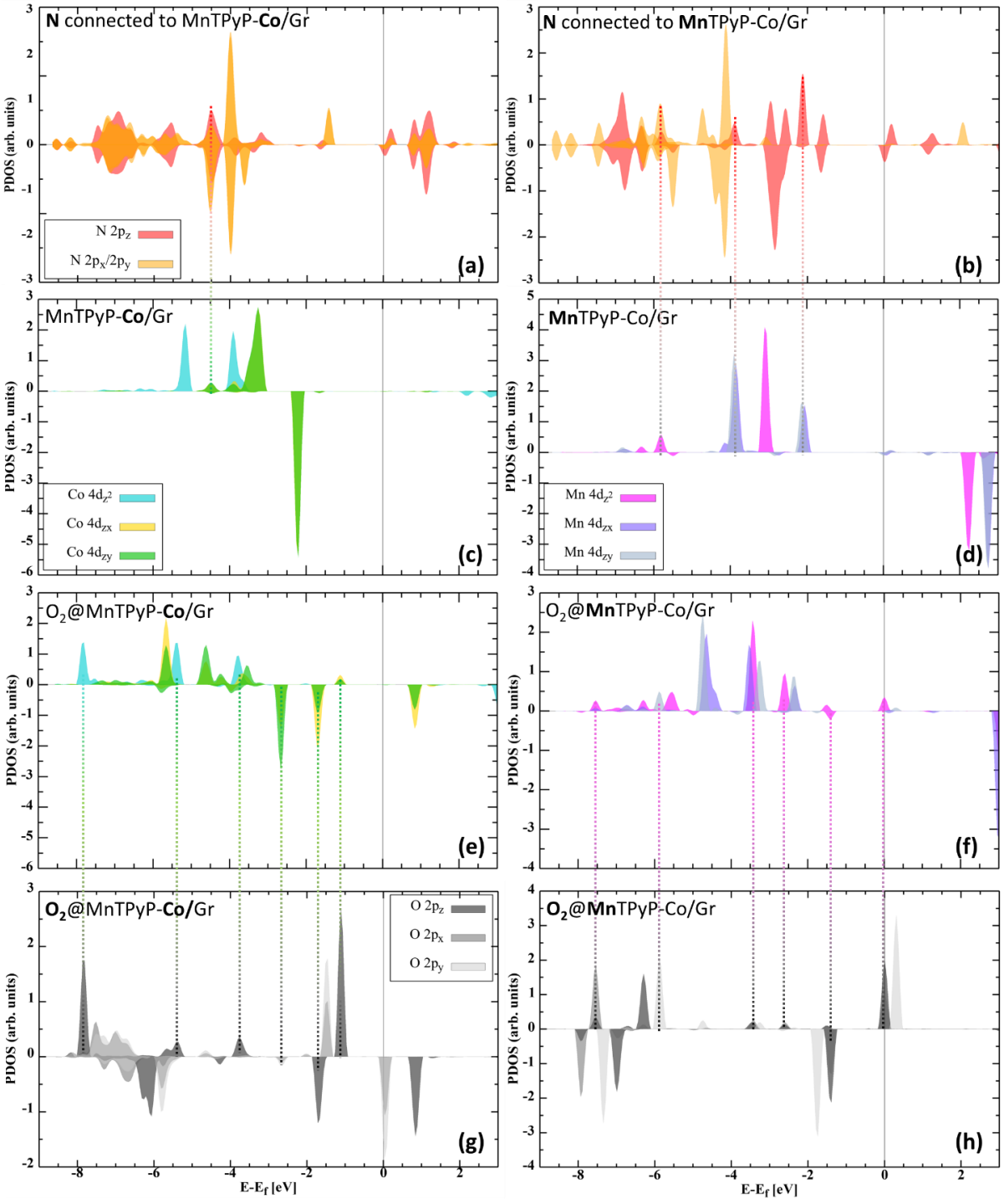

Figure S7. Atom/orbital projected, spin resolved density of states of (a) N connected to Co (c) Co 3d in pristine MnTPyP-Co/Gr, (e) Co 3*d* after O_2 adsorption and (g) O 2*p* after O_2 adsorption. Similarly (b) N connected to Mn atom, (d) Mn 3d before O_2 adsorption and (f) after O_2 adsorption of Mn 3*d* and (h) O 2*p*.

With reference to the electronic structure of the systems, we add in the following a more detailed description. Mn and Co occupied orbitals are mainly contributed by localized d_{zx}, d_{zy} and d_z^2 and N p orbitals near the Fermi level (which is set to 0 eV). In MnTPyP–Co/Gr, the

central Mn d_{zx} and d_{zy} orbitals strongly interact with the nitrogen p orbitals, whereas the Co d_{zx} and d_{zy} orbitals exhibit minimal hybridization with N p orbitals. This difference is also reflected in the average Mn–N and Co–N bond lengths, which are 2.03 Å and 2.26 Å, respectively. In the free O_2 molecule, both HOMO and LUMO are mostly contributed by O $2p_z$ (shown in Figure S2b). Upon ligation at the Co site, O $2p_z$ and Co d_{zx} and d_{zy} split into discrete levels. New unoccupied states hybrid with O $2p_z$ are formed near the Fermi level, the intensity of the contribution from localized d_z^2, d_{zx} and d_{zy} orbitals decreases and hybridization between bonding Co d_z^2 and C p_z orbitals takes place in the -7.5 to -2.5 eV energy range. A significant evolution of the d_{zx} and d_{zy} peaks intensities above the Fermi level indicates charge transfer from d_{zx} and d_{zy} to the O 2p orbital. When O_2 is adsorbed at the Mn site instead, we can observe only a negligible hybridization between Mn d_z^2 and O p_z near the Fermi level, compared to Co site. This correlates with the O_2 bonding geometries. In the case of Mn, the O_2 molecule interacts in the "end on" configuration, associated to the $2p_z$ orbital hybridization with Mn $3d_z^2$. In the case of O_2 at Co site, instead, the O_2 orientation is perfectly horizontal in H-conf due to prominent Co d_{zx} and d_{zy} and O $2p_z$ orbital hybridization and a reduced Co d_z^2 and O $2p_z$ orbital interaction. One major reason for the negligible Mn d_{zx} and d_{zy} interaction with O $2p_z$ is that these orbitals are already involved in strong covalent bonding with the four nitrogen atoms (N 2p) in the macrocycle.

Beyond orbital hybridization effects, we further examined the d-band center of the metallic site. The d-band center of Mn is located at −4.80 eV in MnTPyP/Gr and at −2.88 eV in MnTPyP–Co/Gr. The substantial upshift of the Mn d-band center upon Co incorporation indicates enhanced electronic interaction, which is expected to strengthen O_2 adsorption at the Mn site. This interpretation is consistent with the significantly improved O_2 adsorption energy observed at the Mn sites in MnTPyP–Co/Gr. However, a direct comparison of the d-band center values of Mn (−2.88 eV) and Co (−3.22 eV) alone does not fully correlate with the observed O_2 reactivity at the Mn and Co sites in MnTPyP–Co/Gr, suggesting that factors beyond the d-band center, such as local coordination environment and spin polarization effects, also play a crucial role.

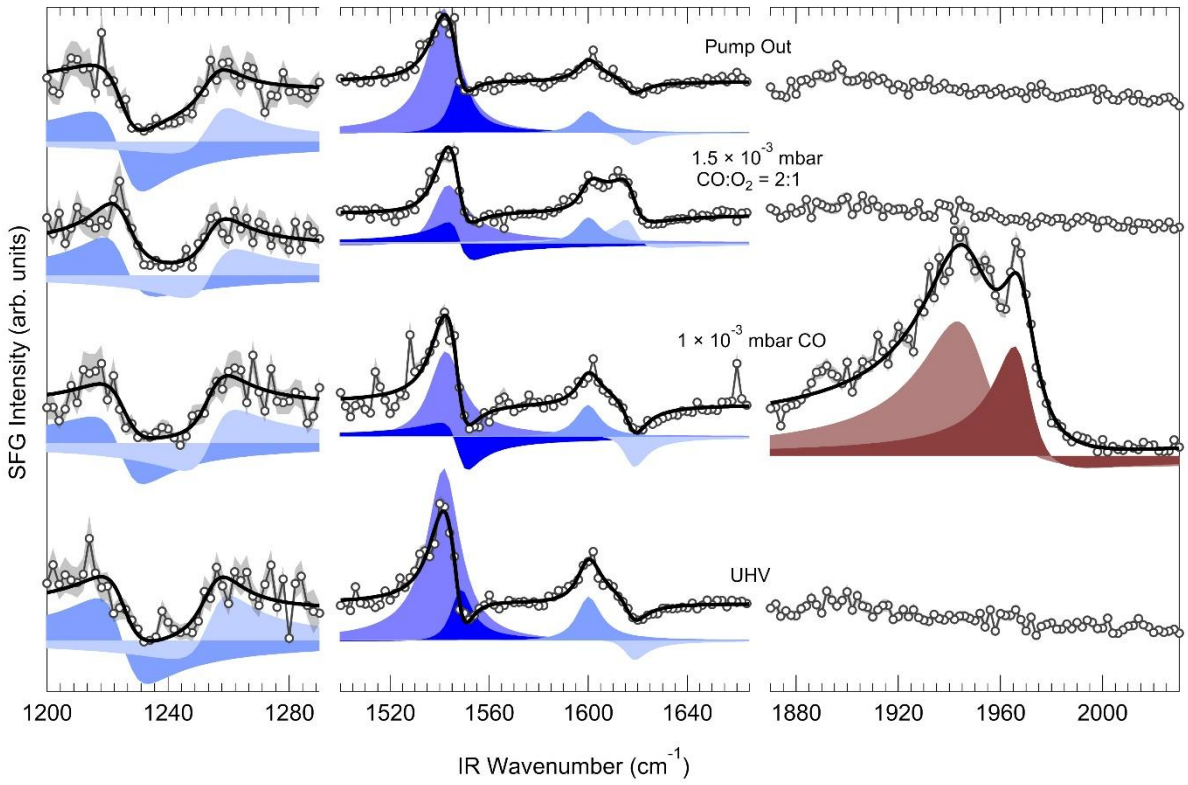

Figure S8. Sum-frequency generation spectra (from bottom up) of the pristine MnTPyP-Co layer in UHV (bottom), in near-ambient pressure of carbon monoxide (10^{-3} mbar), after addition of 0.5×10^{-3} mbar O_2 yielding a $CO:O_2 = 2:1$ pressure ratio, and after recovering UHV conditions (top row). All spectra were collected *in situ* and at room temperature with a visible laser wavelength of 532 nm in the ppp polarization combination (sfg-vis-ir).

MnTPyP	MnTPyP-Co	Mode Assignment
1222		
	1225	δ(pyr)
1243		ν(Cα–N) + δ(Cβ–H), ν(Cm–pur) +
	1257	δ(C–H)pyr
1339		
	1348	ν(Cα–N)
1351		
	1367	
	1419	ν(Cα–N) + δ(Cβ–H), ν(Cα–Cβ)
	1439	
1496		ν(Cα–Cβ), ν(Cβ–Cβ)
	1497	
1522		δ(pyr)
1538		ν(Cβ-Cβ)+δ(Cβ-H), ν(Cβ-Cβ), ν(Cβ-H)
	1539	δ(pyr)
	1546	ν(Cβ-Cβ)+δ(Cβ-H), ν(Cβ-Cβ), ν(Cβ-H)
1559		ν(Cα–Cm), ν(Cm–Cm)
	1595	δ(pyr), ν(C-C)pyr
1599		
	1617	δ(pyr)
1618		Graphene G-mode
2984		
3023		
	3031	ν(Cα–H)
	3063	
3067		
	3090	

Table S1. IR-Vis SFG vibrational resonances positions for the MnTPyP and MnTPyP-Co MOFs on Gr/Ir(111) in cm^{-1} assigned on the basis of our previous work,[1] and by comparison with experimental values for FeTPyP,[2,3] CoTPyP,[4,5] ZnTPyP,[6] 2HTPyP,[7] MnTPPCl,[8] and graphene.[9–11] The vibrational modes notation is the standard used in the literature.[2,3,7]

With reference to the IR-Vis SFG spectra and their oxygen-dependent evolution reported in Figure 5, we add in the following a more detailed description. The features at 1225 and 1255 cm^{-1} are associated with the pyridinic moieties, together with the resonances at 1542, 1600 and 1618 cm^{-1}. The feature at 1548 cm^{-1} could be either associated with a macrocycle mode or to a pyridyl-related one, possibly a chemically shifted counterpart of the resonance at 1542 cm^{-1}, belonging to porphyrins with different peripheral coordination number to Co. The latter resonances are also visible in ssp polarization (Figure 5b). Here, the spectra were fitted by using the same energy and Lorentzian width parameters obtained for the ppp polarization. Upon exposure to 7×10^{-7} mbar O_2, we observe a spectral evolution in both energy ranges and polarizations (central row in Figure 5). These variations are induced by the interaction with oxygen and can be described by the evolution of the phases and amplitudes associated with the resonances, and to a modified non-resonant background. At low energy, exposure to oxygen

leads to a reversible phase rotation of about 50° and −70° paralleled by an amplitude increase of 2 and 4 times, respectively, for the 1225 and 1255 cm^{-1} resonances. The non-resonant background is not significantly affected in this energy range. At higher energy, instead, a slight increase of the non-resonant background amplitude (∼ 20%) is observed in the presence of O_2, recovering upon pump out. Analogously to the low-energy region, the fit results reproduce very well the experimental curves by keeping the energy of the resonances fixed with respect to the pristine layer case, suggesting only a weak gas-layer interaction. In ppp polarization, the amplitude of the resonances at 1542 and 1600 cm^{-1} remains almost constant, as well as the phase of the latter. Instead, the amplitudes associated to the features at 1548 and 1618 cm^{-1} are 1.6 and 4 times larger in oxygen pressure, respectively. All phases, except for the 1600 cm^{-1} resonance, reversibly rotate by about −50° and −60° upon exposure to oxygen. In ssp polarization, the only evident modification from the deconvolution in the central row of Figure 5b involves the 1618 cm^{-1} peak. The two lower energy resonances do not show a significant phase rotation, within our experimental sensitivity to this parameter. Instead, the higher energy resonances show a 45° and −60° phase variation associated to an amplitude increase of 3 and 8 times, in order of increasing energy.

In the case of the high-pressure range (Figure 7), the low-energy resonances are found at 1225 and 1254 cm^{-1}. At higher energy, the resonances are positioned at 1540, 1549, 1612, and 1620 cm^{-1}, with slight energy shifts compared to the previously analyzed layer, associated to small coverage differences depending on the sample preparation. Upon exposure to 1×10^{-3} mbar O_2, the non-resonant amplitude in the 1200 − 1290 cm^{-1} range decreases by about 20%. An additional 10% amplitude loss is observed upon increasing the pressure at 1 mbar. Such a result already differs from the low-pressure measurements where the background reversibly increased in oxygen pressure, witnessing a different electronic structure evolution. In addition, the resonant phases associated with the resonances at 1225 and 1254 cm^{-1}, respectively, rotate by about −80° and +40° after exposure to O_2. The latter resonance amplitude evolves accordingly, more than doubling upon exposure to 10^{-3} mbar O_2. Instead, the former resonant amplitude is about halved at 10^{-3} mbar and further halved at 1 mbar. At higher energy, the background is only affected upon exposure to 1 mbar O_2, by a ∼ 8% reduction. Once again, amplitudes and phases are fitted independently, while the frequencies and widths are globally fitted. The two resonances below 1550 cm^{-1} display a double rotation from UHV to 10^{-3} mbar, and from 10^{-3} to 1 mbar. The phase associated to the 1540 cm^{-1} resonance rotates by −70° first and then by +20°. The one relative to the 1549 cm^{-1} peak changes similarly, with a first rotation of −50° and a second one of +30°, clearly showing a progressive evolution, coupled to the intensity increase. The evolution of the features at 1612 and 1620 cm^{-1} is more dramatic. The former is practically zero in the pristine spectrum, while upon exposure to oxygen its amplitude becomes 3 and 15 times larger, at increasing pressure steps. The almost zero amplitude of this peak in UHV makes its phase insignificant. Instead, a rotation of about 175° is observed from 10^{-3} to 1 mbar O_2. Moreover, the 1620 cm^{-1} resonance evolves by −30° and −60° in consecutive steps, while the amplitude doesn't vary as much.

Co 2p3/2			
UHV	$p_{O_2} = 3 \times 10^{-8}$ **mbar**	***Co(II)TPyP***[12]	***Co(II)O***[13–15]
778.5*	778.5*	779.4*	
780.2	780.2	780.1	780.0
	781.4		781.0-781.2
782.1	782.1	782.1	781.7-782.1
	783.1		
784.8	784.8	784.3	785.5-786.5
O 1s			
$p_{O_2} = 3 \times 10^{-8}$ **mbar**	***CoO***[16,17]	***O/Gr***[18,19]	***O_2***[17,20–22]
529.7	529.5-530.2		$529.6\text{-}530.5_c$
531.2		531.1-531.2	$530.9\text{-}532.1_c$
532.9			
			$535.8\text{-}536.9_p$
			539_g

Table S2. Experimental binding energies, in eV, of Co $2p_{3/2}$ and O 1s spectral components of a MnTPyP-Co/Gr monolayer as-prepared in UHV and in 3×10^{-8} mbar O_2. The Co $2p_{3/2}$ GS peak is identified by a *. The experimental values are assigned to the corresponding species and compared to literature. O/Gr refers to epoxy, enolate and ether species. O_2 refers to molecular oxygen in the gas phase (g), physisorbed (p) or chemisorbed (c) at a metal atom. Concerning the chemisorbed species, the first line refers to O_2^{2-} (peroxo) and the second to O_2^- (superoxo).

References.

[1] S. Baronio, M. De Col, A. Yadav, B. Roondhe, V. Mischke, O. Resel, D. Bidoggia, A. Namar, N. Vinogradov, M. Scardamaglia, M. Valvidares, P. Gargiani, M. Cinchetti, G. Zamborlini, P. Giannozzi, E. Vesselli, "Single atom coordination in a manganese–cobalt bi-metallic framework on graphene: geometric and electronic structures" *Nanoscale* **2025**, *17*, 16946–16963.

[2] S. Popovici, W. Leyffer, R. Holze, "The mechanism of dioxygen reduction at iron meso-tetrakis (pyridyl) porphyrin: a spectroelectrochemical study" *J. Porphyr. Phthalocyanines* **1998**, *2*, 249–260.

[3] N. Blom, J. Odo, K. Nakamoto, D. P. Strommen, "Resonance Raman studies of metal tetrakis(4-N-methylpyridyl)porphine: band assignments, structure-sensitive bands, and species equilibria" *J. Phys. Chem.* **1986**, *90*, 2847–2852.

[4] F. Armillotta, D. Bidoggia, S. Baronio, A. Sala, R. Costantini, M. dell'Angela, I. Cojocariu, V. Feyer, A. Morgante, M. Peressi, E. Vesselli, "Co(III), Co(II), Co(I): Tuning Single Cobalt Metal Atom Oxidation States in a 2D Coordination Network" *Adv. Funct. Mater.* **2024**, *34*, 2408200.

[5] F. Armillotta, A. Pividori, M. Stredansky, N. Seriani, E. Vesselli, "Dioxygen at Biomimetic Single Metal-Atom Sites: Stabilization or Activation? The Case of CoTPyP/Au(111)" *Top. Catal.* **2020**, *63*, 1585–1595.

[6] K. Araki, P. S. Santos, L. F. C. C. de Oliveira, H. E. Toma, "Resonance Raman Spectra of a Supramolecular Species Containing Four Ruthenium(II)-Bipyridine Complexes Attached to Zinc-Tetrapyridyl Porphynate" *Spectrosc. Lett.* **1995**, *28*, 119–126.

[7] J. R. T. Dos Reis, F. F. Leite, K. Sharma, G. A. S. Ribeiro, W. H. N. Silva, A. A. Batista, A. R. Paschoal, W. Paraguassu, M. Mazzoni, N. M. Barbosa Neto, P. T. Araujo, "Raman Spectroscopy on Free-Base Meso-tetra(4-pyridyl) Porphyrin under Conditions of Low Temperature and High Hydrostatic Pressure" *Molecules* **2024**, *29*, 2362.

[8] S. R. Alharbi, A. A. A. Darwish, S. E. Al Garni, H. I. ElSaeedy, K. F. Abd El-Rahman, "Influence of thickness and annealing on linear and nonlinear optical properties of manganese (III) chloride tetraphenyl porphine (MnTPPCl) organic thin films" *Infrared Phys. Technol.* **2016**, *78*, 77–83.

[9] A. A. Taleb, G. Anemone, D. Farías, R. Miranda, "Resolving localized phonon modes on graphene/Ir(111) by inelastic atom scattering" *Carbon* **2018**, *133*, 31–38.

[10] R. Beams, L. G. Cançado, L. Novotny, "Raman characterization of defects and dopants in graphene" *J. Phys. Condens. Matter* **2015**, *27*, 083002.

[11] M. Corva, F. Mohamed, E. Tomsic, M. Rinaldi, C. Cepek, N. Seriani, M. Peressi, E. Vesselli, "Learning from Nature: Charge Transfer and Carbon Dioxide Activation at Single, Biomimetic Fe Sites in Tetrapyrroles on Graphene" *J. Phys. Chem. C* **2019**, *123*, 3916–3922.

[12] F. Armillotta, D. Bidoggia, P. Biasin, A. Annese, A. Cossaro, A. Verdini, L. Floreano, M. Peressi, E. Vesselli, "Spectroscopic fingerprints of iron-coordinated cobalt and iron porphyrin layers on graphene" *Cell Rep. Phys. Sci.* **2023**, 101378.

[13] M. C. Biesinger, B. P. Payne, A. P. Grosvenor, L. W. M. Lau, A. R. Gerson, R. S. C. Smart, "Resolving surface chemical states in XPS analysis of first row transition metals, oxides and hydroxides: Cr, Mn, Fe, Co and Ni" *Appl. Surf. Sci.* **2011**, *257*, 2717–2730.

[14] A. A. Khassin, T. M. Yurieva, V. V. Kaichev, V. I. Bukhtiyarov, A. A. Budneva, E. A. Paukshtis, V. N. Parmon, "Metal–support interactions in cobalt-aluminum co-precipitated catalysts: XPS and CO adsorption studies" *J. Mol. Catal. Chem.* **2001**, *175*, 189–204.

[15] C. Song, H. Luo, X. Duan, Y. Li, Y. Li, Y. Yang, J. Wu, F. Wang, F. Meng, J. Zhang, "Ultrafine cobalt oxide nanosheets for enhanced high activity towards oxygen evolution reaction" *Catal. Commun.* **2022**, *171*, 106520.
[16] J. Haber, J. Stoch, L. Ungier, "X-ray photoelectron spectra of oxygen in oxides of Co, Ni, Fe and Zn" *J. Electron Spectrosc. Relat. Phenom.* **1976**, *9*, 459–467.
[17] B. Bozzini, A. Previdi, M. Amati, M. Bevilacqua, G. Cordaro, M. Corva, A. Donazzi, G. Dotelli, L. Gregoratti, R. Pelosato, M. Vorokhta, E. Vesselli, "In situ near-ambient pressure X-ray photoelectron spectroscopy discloses the surface composition of operating NdBaCo2O5+δ solid oxide fuel cell cathodes" *J. Power Sources* **2019**, *436*, 226815.
[18] S. Kyrkjebø, A. Cassidy, N. Akhtar, R. Balog, M. Scheffler, L. Hornekær, B. Holst, R. Flatabø, "Graphene and graphene oxide on Ir(111) are transparent to wetting but not to icing" *Carbon* **2021**, *174*, 396–403.
[19] N. A. Vinogradov, K. Schulte, M. L. Ng, A. Mikkelsen, E. Lundgren, Ma, A. B. Preobrajenski, "Impact of atomic oxygen on the structure of graphene formed on Ir(111) and Pt(111)" *J. Phys. Chem. C* **2011**, *115*, 9568–9577.
[20] B. Eren, C. Heine, H. Bluhm, G. A. Somorjai, M. Salmeron, "Catalyst Chemical State during CO Oxidation Reaction on Cu(111) Studied with Ambient-Pressure X-ray Photoelectron Spectroscopy and Near Edge X-ray Adsorption Fine Structure Spectroscopy" *J. Am. Chem. Soc.* **2015**, *137*, 11186–11190.
[21] C. Puglia, A. Nilsson, B. Hernnäs, O. Karis, P. Bennich, N. Mårtensson, "Physisorbed, chemisorbed and dissociated O2 on Pt(111) studied by different core level spectroscopy methods" *Surf. Sci.* **1995**, *342*, 119–133.
[22] C. T. Campbell, "An XPS study of molecularly chemisorbed oxygen on Ag(111)" *Surf. Sci.* **1986**, *173*, L641–L646.